Supercritical rotating flow over topography

J. G. Esler,[a] O. J. Rump, and E. R. Johnson
Department of Mathematics, University College London, London WC1E 6BT, United Kingdom

(Received 7 November 2008; accepted 2 April 2009; published online 18 June 2009)

The flow of a one-and-a-half layer Boussinesq fluid over an obstacle of nondimensional height M, relative to the lower layer depth, is investigated in the presence of rotation, the magnitude of which is measured by a nondimensional parameter B (inverse Burger number). The supercritical regime in which the Froude number F, the ratio of the flow speed to the interfacial gravity wave speed, is significantly greater than one is considered in the shallow water (small aspect ratio) limit. The linear drag exerted by the obstacle on the flow is shown to be $M^2/(F\sqrt{F^2-1})\times f(B/F^2-1)$, where f is a function specific to each obstacle. Explicit expressions are given for several common obstacle shapes, and the results are checked against nonlinear flows simulated by a shock-capturing finite volume numerical scheme. For flows within the supercritical regime ($F-1\gg M^{2/3}$) the linear drag result is found to remain accurate up to (at least) $M\approx 0.7$. The success of the linear drag theory can be explained because, in the supercritical regime, strong nonlinearities are displaced to the wake regions at the flanks of the obstacle. In the presence of weak rotation and for small obstacle height the development of the nonlinear wakes is governed by the Ostrovsky–Hunter (OH) equation. Across a wide range of parameter space the wake pattern is determined by a single parameter $\beta=3M/B\sqrt{F^2-1}$. Numerical solutions of the OH equation illustrate the dependence of flow patterns and wave breaking regions on β. Results are again verified by comparison with numerical solutions of the full nonlinear rotating shallow water equations. © *2009 American Institute of Physics*.
[DOI: 10.1063/1.3139306]

I. INTRODUCTION

Rotating stratified flows over obstacles are ubiquitous in the atmosphere and oceans. Understanding the fundamental processes occurring in such flows is essential if the influence of topography on the larger-scale flow is to be modeled accurately. In particular the drag on the flow generated by subgrid scale topography must be parametrized in numerical weather prediction and climate models. The focus in the development of such parametrization has naturally been on the generation and influence of vertically propagating inertia-gravity waves because of their importance for the momentum budget of the upper atmosphere. However, for general upstream wind and buoyancy profiles, not all waves generated by flow over topography are free to propagate vertically. Wave energy may become "vertically trapped" in horizontal wave guides which owe their existence to, for example, local discontinuities or sharp gradients in the buoyancy field, or alternatively to turning surfaces generated by strong vertical shear in the horizontal wind field.[1–3] Trapped waves can be resonantly excited by topographic forcing, leading to the generation of nonlinear waves with significant amplitude, as is apparent in the compelling pictures derived from synthetic aperture radar measurements of flow over St. Lawrence island (170 °W, 63.5 °N) by Li *et al.*[4]

Numerical and analytical studies[5,6] indicate that the effect of rotation on high Froude number (linear) stratified flow over isolated three-dimensional obstacles is generally to reduce the drag exerted by the obstacle on the flow. The current work aims to determine whether or not similar conclusions hold for vertically trapped waves, and to develop qualitative and quantitative understanding of the behavior of the waves excited by an isolated topographic obstacle in a rotating flow with a single active layer. The focus is on the supercritical regime in which the Froude number F, defined as the ratio of the oncoming flow speed to the characteristic gravity wave phase speed,[7] is greater than unity. Following previous studies,[8–12] the rotating shallow water equations (rSWEs) are chosen as a model paradigm that can be regarded as representative of more general atmospheric and oceanic flows. For the atmosphere the physically relevant scenario described by the rSWE is that of a Boussinesq one-and-a-half layer fluid, in which a layer of finite depth underlies an infinite layer of slightly greater buoyancy. Here, the focus is on the relatively simple scenario with a uniform background flow in both layers because if shear is present between the layers geostrophic balance would require the interface between the layers to slope. Under the shallow water approximation the infinite upper layer remains dynamically passive apart from the uniform flow. The horizontal wave guide in this flow is simply the interface between the layers, and all waves generated by the topography consequently remain vertically trapped and propagate horizontally on this interface. Note that in the meteorological terminology, a mountain wave is defined as being trapped if the "Scorer parameter," which is in fact a function of height z that corresponds to the vertical wavenumber in the Wentzel–Kramers–Brillouin (WKB) solution, becomes negative anywhere aloft in the flow. Here, the simpler situation of waves

[a]Author to whom correspondence should be addressed. Electronic mail: gavin@math.ucl.ac.uk.

being trapped on the interface between the two layers is proposed as a prototype for all vertically trapped waves, although clearly further work will be required to determine if the qualitative behaviors discovered apply equally to waves trapped by other mechanisms.

The main focus here will be on answering the following questions:

- What is the drag exerted by the obstacle on the flow in the supercritical regime? In particular, how is the drag influenced by rotation? How does the drag due to horizontally trapped waves compare to that generated by vertically propagating waves in a comparable continuously stratified flow?
- What determines the occurrence of wave breaking, and the location of wave breaking regions, in the wakes of rotating supercritical flows? In the absence of other mechanisms of wave dissipation, wave breaking causes the deposition of horizontal momentum transported by the waves generated at the obstacle, and understanding this process is the key to understanding the influence of the obstacle on the wider fluid flow.

In order to understand the occurrence of the supercritical flows of interest here, it is helpful to invoke the close analogy between the problems of nonrotating flow over an obstacle and flow past an aerofoil in compressible gas dynamics. Jiang and Smith[10] illustrated numerically the presence of "bow shocks" when the Froude number F is relatively close to unity (cf. transonic flow), and their absence in flows with Froude number much greater than unity (cf. supersonic flow). In the "supercritical flows" with $F \gg 1$ the disturbance to the oncoming stream due to the obstacle was found to consist only of "V-waves," aligned along Mach lines emanating behind the obstacle at angles $\pm\tan^{-1}(\sqrt{F^2-1})$. Esler *et al.*[12] (ERJ07a hereafter) used matched asymptotics to show that the boundary between the transcritical and supercritical regimes, in terms of the nondimensional obstacle height M, occurs in (M,F) parameter space near the curve $F=1+\Gamma^+M^{2/3}$, where Γ^+ is an obstacle dependent positive constant taking a value near unity. Numerical simulations showed the transition between the two regimes to be abrupt. The effect of rotation on transcritical flows has been studied in detail elsewhere (Esler *et al.*,[13] ERJ07b hereafter), and consequently the aim of the present work is to determine its effect in the supercritical regime, where $F \gtrsim 1+\Gamma^+M^{2/3}$.

In Sec. II the physical situation and appropriate model equations for one-and-a-half layer flow over an isolated obstacle, the rSWE, are introduced. The shock-capturing finite volume numerical method used to obtain nonlinear solutions of the rSWE is then described. In Sec. III, the steady linear behavior of the rSWE solutions, valid when rotating effects are relatively strong compared to topographic forcing, is described and a new expression for the drag exerted on the flow by an axisymmetric obstacle of fixed height and volume is expressed in terms of the obstacle's radial profile. In Sec. IV a nonlinear equation for the wake behavior in the presence of weak rotation is derived. The conditions that determine the occurrence and location of wave breaking are elucidated. Finally, in Sec. V, conclusions are given.

II. MODEL EQUATIONS AND NUMERICAL SOLUTION

A. Physical scenario and model equations

The physical scenario to be modeled is that of a one-and-a-half layer inviscid fluid, consisting of a layer of undisturbed depth H and uniform density ρ_2 underlying a less dense layer (density ρ_1) of infinite vertical extent. For ease of exposition the density difference is taken to be small, hence $(\rho_2-\rho_1)/\rho_2 \ll 1$ and the Boussinesq approximation can be made. The fluid, acted on by gravity g, rotates at angular frequency $f/2$ and both layers flow with an initially uniform speed U, which is taken to be from right to left, over an obstacle with maximum height h_m and horizontal scale L. Further, the aspect ratio of the flow is taken to be small $(H/L \ll 1)$ so that shallow water dynamics applies in the lower dynamically active layer, and to leading order the flow remains uniform in the upper layer for all time.

It is straightforward to show that the nondimensional rSWEs hold for the lower layer flow, i.e.,

$$\begin{aligned} &u_t + (u-F)u_x + vu_y - \sqrt{B}v = -\sigma_x - Mh_x, \\ &v_t + (u-F)v_x + vv_y + \sqrt{B}u = -\sigma_y - Mh_y, \\ &\sigma_t + ((u-F)\sigma)_x + (v\sigma)_y = 0, \end{aligned} \tag{1}$$

where σ is the layer thickness, $h=h(x,y)$ is the topography, and the total horizontal velocity is $\mathbf{u}=(-F+u,v)$. Equation (1) has been nondimensionalized by taking the horizontal length scale to be L, the horizontal velocity scale to be $c \equiv \sqrt{g'H}$ (the long interfacial gravity wave speed in the absence of rotation), the time scale to be L/c, and the layer thickness scale to be H. Three nondimensional parameters now appear explicitly in Eq. (1): The Froude number $F=U/c$, the nondimensional obstacle height $M=h_m/H$, and an inverse Burger number $B=f^2L^2/c^2$. Note that B is the square of the ratio of the obstacle length scale L to the radius of deformation $L_R=c/f$. Results are presented in terms of F, M, and B in all that follows.

Following Houghton,[14] and as in ERJ07a, the physical situation at breaking waves is modeled by allowing "weak" or discontinuous solutions of Eq. (1) that include the possibility of mass and (lower layer) momentum conserving hydraulic jumps, as discussed by Klemp *et al.*[15] The discontinuous solutions must satisfy the Rankine–Hugoniot conditions

$$\begin{aligned} &-V[\sigma]_-^+ + [\sigma\mathbf{u}\cdot\mathbf{n}]_-^+ = 0, \\ &-V[\sigma\mathbf{u}\cdot\mathbf{n}]_-^+ + \left[\sigma(\mathbf{u}\cdot\mathbf{n})^2 + \tfrac{1}{2}\sigma^2\right]_-^+ = 0, \end{aligned} \tag{2}$$

where $\mathbf{n}$ is a horizontal unit vector normal to the jump, V is the jump speed in the direction of $\mathbf{n}$, and $[\cdot]_-^+$ denotes the difference between the evaluated quantity in brackets upstream and downstream of the jump.

Klemp *et al.*[15] noted that condition (2), which is derived for the one-and-a-half layer system under the assumption of energy dissipation occurring in the lower layer only (see also

Ref. 16, p. 67), is appropriate for standing hydraulic jumps, such as those generated by flow over the isolated obstacles as studied here. There is an implicit assumption made in using Eq. (2), of wave breaking and turbulence at the hydraulic jump, which is experimentally observed for jumps of sufficient amplitude. For low jumps there is a possibility of significant energy and momentum transport out of the jump by internal waves, a possibility that will not be addressed here. Figure 16 of Klemp *et al.*[15] showed that the assumption of lower layer energy dissipation is quantitatively accurate in a numerical simulation of a typical standing hydraulic jump in a Boussinesq nonhydrostatic flow. It is important to note that condition (2) is not appropriate for traveling internal bores or gravity currents, and there are numerous other suggestions for jump conditions in those scenarios, see the discussions in Refs. 15 and 17.

B. Numerical solution of the rotating shallow water equations

Numerical solutions of the nonlinear rSWE are presented below. Following Esler *et al.*,[13] the finite volume software package conservation laws software package[18] (CLAWPACK) is used to obtain the solutions. Explicit details of how CLAWPACK can be adapted to solve the shallow water equations in two dimensions are given by LeVeque,[18] and here the rotation and topographic forcing terms are treated using the method of Strang splitting, following Kuo and Polvani.[19] Note that however, accurate new methods for the treatment of nonconservative forcing terms in this problem have recently been developed.[20,21] The reader is referred to ERJ07a and ERJ07b for discussion of some of the technical issues arising in the application of the above algorithm to the particular problem of flow over an isolated obstacle, and details of the convergence tests performed to verify results. Notably, the variable domain size requirements found necessary to simulate the transcritical flows investigated in ERJ07a and ERJ07b, in which $F\sim 1$, do not need as much consideration in obtaining solutions for the supercritical rotating flows described here. Here, a constant domain size of $10L\times 10L$ is found to be adequate for convergence of the calculations of drag presented in Sec. III. A larger domain size $(15L\times 30L)$ is used to obtain the profiles of the interface displacement field $\eta(x,y)$ shown below. A grid spacing $\delta x=0.01L$ is used throughout. The model is integrated forward in time with an adjustable time step based on the Courant–Friedrichs–Lewy criterion (for details, see Ref. 18) until the flow in a predetermined region around the obstacle converges to satisfy a steady state numerical criterion. Further details are given in Rump's thesis.[22]

III. LINEAR THEORY AND THE LINEAR DRAG EXERTED BY THE OBSTACLE

A. Steady solutions in Green's function form

Linearizing the rotating shallow water Eq. (1), the following equation for the interface displacement $\eta=\sigma-1+Mh$ is obtained,

$$((\partial_t - F\partial_x)^2 - \nabla^2 + B)\,\eta = M((\partial_t - F\partial_x)^2 + B)h. \tag{3}$$

The term involving the topography $Mh(x,y)$ can be considered to be a forcing term, generating a response in the interface η. For an obstacle with comparable dimensions in the along and cross-stream directions, Eq. (3) is formally valid when $M \ll \min\{1,(F-1)^{3/2}\}$, with the transcritical theory discussed in ERJ07a (Ref. 12) and ERJ07b (Ref. 13) being valid when $M\sim(F-1)^{3/2}\ll 1$.

Steady solutions to Eq. (3) can be obtained in Green's function form. Vilenski and Johnson[23] addressed the closely related problem of flow over an anisotropic obstacle, with a cross-stream scale $\sim M^{-1/2}\times$ its along-stream scale, in the Kadomtsev–Petviashvili limit,[24,25] given by $F\to 1$, $M\to 0, (F-1)/M^{1/2}\to$const. The Green's function solution for Eq. (3) can be obtained by adapting the results of Vilenski and Johnson.[23] Note that the same equation for steady flow results from Eq. (3) regardless of whether the flow over the obstacle is right to left (as here) or left to right. As the system is hyperbolic, the correct causality or wave radiation conditions must be imposed in order to obtain a uniquely valid expression in each case, just as for Green's function solutions of the wave equation (e.g., Morse and Flesbach[26]). Adapting these previous results, the Green's function solution to Eq. (3) for a right-to-left basic flow is

$$\eta(\mathbf{x}) = M\int (F^2 h_{xx}(\mathbf{x}-\mathbf{x}') + Bh(\mathbf{x}-\mathbf{x}'))G(\mathbf{x}')d^2\mathbf{x}', \tag{4}$$

where $\mathbf{x}=(x,y)$ and $\mathbf{x}'=(x',y')$. The Green's functions is given by[23]

$$G(x,y) = \begin{cases} \dfrac{1}{2\sqrt{F^2-1}}\, J_0\left(\dfrac{\sqrt{B}\sqrt{x^2-(F^2-1)y^2}}{\sqrt{F^2-1}}\right), & x\in\mathcal{R} \\ 0, & x\notin\mathcal{R}. \end{cases} \tag{5}$$

where $\mathcal{R}$ is the wedge-shaped region $x<0$, $x^2>(F^2-1)y^2$. Note that it is in fact unhelpful to attempt to simplify Eq. (4) using integration by parts, and then redefining the Green's functions so that only h appears in Eq. (4). Following such a procedure, the redefined Green's function is singular along the Mach lines $x=\pm\sqrt{F^2-1}y$, and consequently both its interpretation and its direct quadrature become more difficult.

The Green's function solution (4) for the Witch of Agnesi (WA) obstacle defined in Table I, and with $(F,B)=(1.3,0.72)$, is shown in Fig. 1 (left). The steady interface displacement field $\eta(x,y)$ is obtained by direct quadrature of Eq. (4). The solution attains maximum amplitude along the Mach lines $x=\pm\sqrt{F^2-1}y$ extending from the obstacle. Relatively long waves are also excited throughout the region bounded by these Mach lines. This pattern is typical of those generated from linear solutions given by Eq. (4).

B. Comparison between linear and nonlinear solutions

To develop insight into the utility of linear theory, it is helpful to compare the Green's function solution in Fig. 1 (left) with a nonlinear solution. Figure 1 (right) shows a nu-

TABLE I. Example obstacle shapes, their Hankel (Fourier–Bessel) transforms, and the corresponding function $f(s)$ giving the dependence of the drag D on the rotation rate and flow speed The five obstacles have unit height and are normalized to have the same volume as the PB ($V=\pi/2$) using the stated value of the nondimensional constant a. $J_n(z)$ is the Bessel function of the first kind of order n, $K_n(z)$ is the modified Bessel function of the first kind, $H_n(z)$ is the Struve function of order n, and ${}_1F_2(a_1;b_1,b_2,z)$ is the generalized hypergeometric function.

Obstacle	$h(r)$	$\hat{h}(\kappa)$	f (s)
Witch of Agnesi ($a=1/2$)	$\frac{a^3}{(a^2+r^2)^{3/2}}$	$a^2\exp(-a\kappa)$	$a^4s^3K_1(2as)+\frac{1}{2}a^3s^2K_2(2as)$
Gaussian ($a=1/\sqrt{2}$)	$\exp\left\{-\frac{r^2}{a^2}\right\}$	$\frac{a^2}{2}\exp\left(-\frac{1}{4}a^2\kappa^2\right)$	$\frac{\sqrt{\pi}a}{4\sqrt{2}}(1+a^2s^2)\exp\{-a^2s^2/2\}$
Cone ($a=\sqrt{3/2}$)	$1-\frac{r}{a}\quad(r<a)$	$\frac{\pi}{2\kappa^2}(J_1(a\kappa)H_0(a\kappa)-J_0(a\kappa)H_1(a\kappa))$	No closed form expression found
Hemiellipsoid ($a=\sqrt{3}/2$)	$\sqrt{1-\frac{r^2}{a^2}}\quad(r<a)$	$\frac{1}{a\kappa^3}(\sin(a\kappa)-a\kappa\cos(a\kappa))$	$\frac{\pi a}{6}\left(6\,{}_1F_2\left(\frac{1}{2};\frac{3}{2},4;-a^2s^2\right)-2\,{}_1F_2\left(\frac{1}{2};2,\frac{5}{2};-a^2s^2\right)-3J_0(2as)-2a^2s^2\,{}_1F_2\left(\frac{3}{2};2,\frac{5}{2};-a^2s^2\right)\right)$
Paraboloid	$1-r^2\quad(r<1)$	$\frac{2}{\kappa^2}J_2(\kappa)$	$\frac{1}{s^3}(6H_2(2s)-2sH_1(2s))$

merical solution of the rSWE at parameter settings $(F,B,M)=(1.3,0.72,0.1)$, allowing direct comparison between nonlinear flows at a relatively low obstacle height with the corresponding linear solution. Directly above the obstacle, the interface displacements are similar, but it is clear that in the wake to the flanks of the obstacle nonlinearity has a pronounced effect. In the nonlinear flow two hydraulic jumps are present in the wake at each side of the obstacle. Symmetry between the wakes at the two sides of the obstacle is broken by nonlinearity, but at the low obstacle height $M=0.1$ shown here, and indeed throughout the supercritical regime, the asymmetry is found to be small.

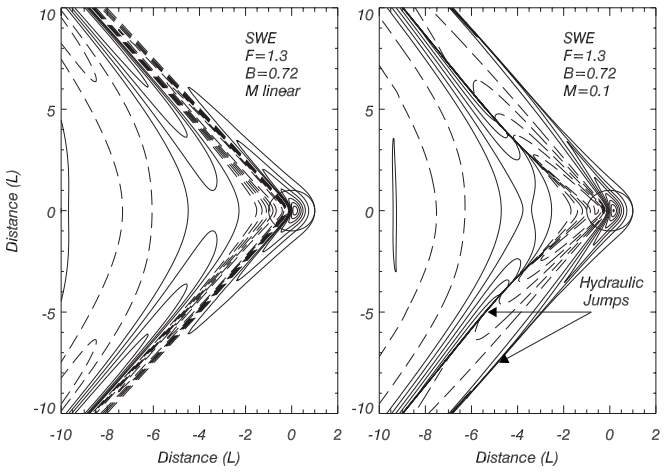

FIG. 1. A comparison of the steady interface displacement field $\eta(x,y)$, for linear and nonlinear solutions of the rSWEs, for flow over the WA obstacle. The flow parameters are set to $(F,B)=(1.3,0.72)$ and $M\to 0$ for the linear solution (left panel) and $M=0.1$ for the nonlinear solution (right panel). The contour interval is $0.15M$ in each case, with negative contours dashed and the zero contour omitted. Note the hydraulic jumps appearing in the nonlinear obstacle wake.

The displacement of the essential nonlinear effects to the wake at the flanks of the obstacle, as in Fig. 1 (right), is used as the definition of the supercritical regime of rSWE flow over obstacles in ERJ07b.[13] In the supercritical regime the two hydraulic jumps can be considered to be "rotation modified" versions of the N-waves of Whitham,[27] that have been shown to characterize the wakes of nonrotating shallow water flows over isolated obstacles.[10,12] The fact that the nonlinearity is displaced away from the obstacle in this fashion suggests that linear theory will accurately capture the drag exerted by the obstacle on the flow, as will be demonstrated next.

C. Drag in steady rotating flow

The aim here is to derive a general expression for the steady state drag over an isolated obstacle of circular cross section. A Fourier transform approach is used, in order to exploit Parseval's theorem. Following Lighthill,[28] a useful device to ensure the correct causality, when transforming to Fourier space, is to assume an exponentially growing obstacle of the form

$$h(x,y,t)=\frac{1}{2\pi}\int_{-\infty}^{\infty}\int_{-\infty}^{\infty}\hat{h}(k,l)\exp\{i(kx+ly)+\epsilon t\}dkdl. \quad (6)$$

In the limit $\epsilon\to 0$ the solution converges to the steady state solution at $t=0$, with $\epsilon>0$ consistent with the solution including only waves radiating outward from the obstacle (as opposed to inwards from infinity). Seeking a solution of Eq. (3) of the form

$$\eta(x,y,t)=\frac{1}{2\pi}\int_{-\infty}^{\infty}\int_{-\infty}^{\infty}\hat{\eta}(k,l)\exp\{i(kx+ly)+\epsilon t\}dkdl$$

results in

$$\hat{\eta}(k,l) = \lim_{\epsilon \to 0} M\hat{h}(k,l)\frac{(\epsilon - ikF)^2 + \nu^2}{(\epsilon - ikF)^2 + \nu^2 + k^2 + l^2}. \quad (7)$$

The linear drag exerted by the obstacle on the flow in steady state is given by[10]

$$D = -M\int_{-\infty}^{\infty}\int_{-\infty}^{\infty}\eta h_x dxdy = -M\int_{-\infty}^{\infty}\int_{-\infty}^{\infty} ik\hat{\eta}\hat{h}^* dkdl, \quad (8)$$

where Parseval's theorem is used with Eq. (7) to obtain the second expression, and $*$ denotes the complex conjugate.

Attention is restricted from here onwards to obstacles with circular cross section $h=h(r)e^{\epsilon t}$, where $r^2=x^2+y^2$. A standard result (e.g., Gradshteyn and Ryzhik,[29] p. 953) is that the two-dimensional Fourier transform of an axisymmetric function reduces to a one-dimensional Hankel or Fourier–Bessel transform,

$$\hat{h}(k,l) = \frac{1}{2\pi}\int_{-\infty}^{\infty}\int_{-\infty}^{\infty} h(r)\exp\{-ikx - ily\}dxdy$$

$$= \hat{h}(\kappa) = \int_0^{\infty} h(r)J_0(\kappa r)rdr,$$

where $\kappa^2=k^2+l^2$. The inverse transform is

$$h(r) = \int_0^{\infty}\hat{h}(\kappa)J_0(\kappa r)\kappa d\kappa.$$

Writing $k=\kappa\cos\theta$, $l=\kappa\sin\theta$ the expression for drag becomes

$$D = -2\pi M^2 i \lim_{\epsilon\to 0}\int_0^{\infty}\kappa^2\hat{h}(\kappa)^2$$

$$\times\int_0^{2\pi}\frac{\cos\theta[(\epsilon - i\kappa F\cos\theta)^2 + B]}{(\epsilon - i\kappa F\cos\theta)^2 + B + \kappa^2}d\theta d\kappa. \quad (9)$$

As $\epsilon\to 0$, $O(\epsilon)$ terms in the numerator and $O(\epsilon^2)$ terms in the denominator may be neglected giving

$$D = -M^2 i\int_0^{\infty}\kappa^2\hat{h}(\kappa)^2 I(\kappa;F,B)d\kappa, \quad (10)$$

where

$$I(\kappa;F,B) = \lim_{\epsilon\to 0}\int_0^{2\pi}\frac{\cos\theta(B - \kappa^2F^2\cos^2\theta)}{-\kappa^2F^2\cos\theta + B + \kappa^2 - 2i\epsilon\kappa F\cos\theta}d\theta. \quad (11)$$

The integral $I(\kappa;F,B)$ can be evaluated using standard complex methods, described in Appendix A, as

$$I(\kappa;F,B) = \begin{cases} \dfrac{2\pi i}{F\sqrt{F^2-1}}\dfrac{\kappa}{\sqrt{\kappa^2 - B/(F^2-1)}}, & \text{for } \dfrac{\kappa F}{\sqrt{B+\kappa^2}} > 1 \\ 0, & \text{for } \dfrac{\kappa F}{\sqrt{B+\kappa^2}} < 1 \end{cases}$$

and consequently the drag D is given by

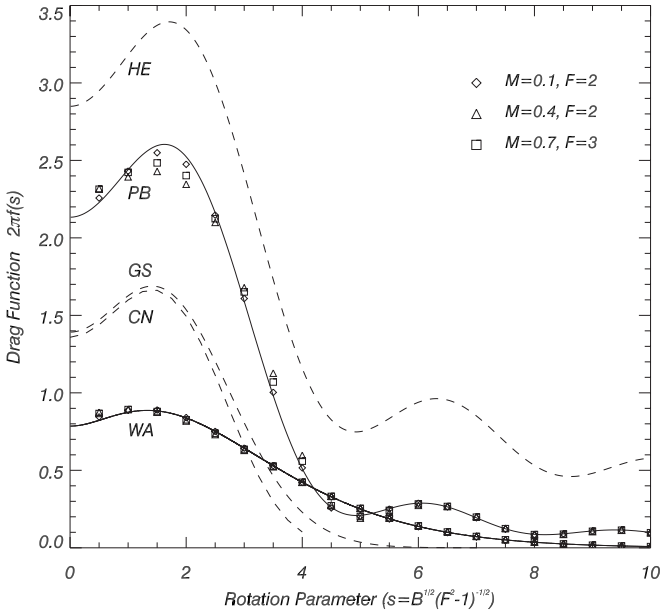

FIG. 2. The drag function $2\pi f(s)$ as a function of the rotation parameter $s=\sqrt{B/(F^2-1)}$ for the obstacles described in Table I.

$$D = \frac{2\pi M^2}{F\sqrt{F^2-1}}f\left(\frac{\sqrt{B}}{\sqrt{F^2-1}}\right). \quad (12)$$

The function f is given by

$$f(s) = \int_s^{\infty}\frac{\hat{h}(\kappa)^2\kappa^3}{\sqrt{\kappa^2 - s^2}}d\kappa \quad (s \geq 0). \quad (13)$$

Equation (12) is a new closed form expression for the drag in linear rotating supercritical flow over an axisymmetric obstacle with radial profile $h(r)$. The result is quadratic in obstacle height M, but exhibits a nontrivial and obstacle-specific functional dependence on the Froude number F and inverse Burger number B. For many common obstacle shapes the integral expression for $f(s)$ can be evaluated explicitly, with several examples being given in Table I. Plots of the resulting functions $f(s)$ are shown in Fig. 2. For most of the obstacles considered $f(s)$ has a maximum around $s=1$ indicating that at fixed Froude number F, drag initially increases with rotation rate, before decreasing rapidly.

For the paraboloid (PB) and "Witch of Agnesi" (WA) obstacles a suite of numerical simulations, using the rSWE finite volume code described above, has been used to test the accuracy of Eq. (12). Three sequences of simulations at fixed $(F,M)=(2,0.1)$, (2, 0.4), and (3, 0.7) were performed, varying B in each case in order to evaluate $f(s)$ for $s=0.5,1,1.5,\ldots,10$. In the simulations, the steady state drags are established within a few advection times (L/c), except for weak vacillations which persist for considerably longer. The wake patterns to the obstacle flanks, at a distance L_w from the obstacle, become established over a longer timescale (proportional to L_w/c).

The drag results in Fig. 2 demonstrate clearly that Eq. (12) is accurate for the drags generated by both obstacles in each family of nonlinear flows, including those for the largest nondimensional mountain height $M=0.7$. In fact, Eq. (12)

more accurately describes the drags in the $(F,M)=(3,0.7)$ set compared to the $(F,M)=(2,0.4)$ set. The reason for this is that the relevant measure of nonlinearity is not solely the nondimensional mountain height, but the distance in parameter space from the transcritical regime [see ERJ07a,[12] ERJ07b (Ref. 13)], which is given approximately by the value of the similarity parameter $\Gamma=(F-1)/M^{2/3}$. The similarity parameter is larger ($\Gamma=2.53$) for the (3,0.7) than for the (2,0.4) set ($\Gamma=1.84$), hence the effects of nonlinearity are stronger for the latter set. Based on the results of ERJ07a,[12] the drag formula (12) is expected to be accurate only for $\Gamma \gtrsim \Gamma^+$, where Γ^+ is an obstacle-specific constant with values typically in the range of 1–1.5.

Note that an alternative expression for the drag in nonrotating flow is given in ERJ07a (Eq. 2.28 therein), as follows:

$$D=\frac{2c_d M^2}{F\sqrt{F^2-1}}, \quad c_d=\int_{-\infty}^{\infty}\mathcal{X}^2 G(\mathcal{X})^2 d\mathcal{X},$$
$$G(\mathcal{X})=\int_{|\mathcal{X}|}^{\infty}\frac{h'(r)}{\sqrt{r^2-\mathcal{X}^2}}dr. \tag{14}$$

Consistency between Eqs. (12) and (14) requires that $\pi f(0)=c_d$, requiring the following integral transform identity to hold

$$\pi\int_0^{\infty}\kappa^2\hat{h}(\kappa)^2 d\kappa = 2\int_0^{\infty}\mathcal{X}^2 G(\mathcal{X})^2 d\mathcal{X}. \tag{15}$$

It is shown in Appendix B that the resulting Eq. (15) holds for any $h(r)$ $(0\le r<\infty)$ for which the Hankel transform exists.

IV. NONLINEAR THEORY AND THE STRUCTURE OF THE WAKE

A. Derivation of a nonlinear equation for the wake

The numerical drag calculations described above indicate that linear drag theory is accurate, even for large amplitude obstacles, in rotating supercritical flow. The linear solution (4) is therefore expected to be accurate in the vicinity of the obstacle, but this does not preclude strong nonlinearity developing in the wake to the obstacle flanks, as seen in Fig. 1. Waves generated at the obstacle will transport pseudomomentum, and this pseudomomentum will be deposited as momentum where those waves are dissipated. To investigate what determines the location of wave breaking and dissipation, a weakly nonlinear description of the developing wake follows.

Solutions of Eq. (1), in the limit $\epsilon \equiv M \ll 1$ are sought in two spatial regions. The first "inner" region has horizontal scale comparable to the obstacle, and is described by coordinates (x,y). The second "outer" region has the scale of the wake, and is described by coordinates $(x_*,y_*)=\epsilon(x,y)$. For the purposes of the asymptotic theory, rotation is taken to be sufficiently weak that $B/M=\nu^2$ (i.e., $\sqrt{B}=\epsilon^{1/2}\nu$), where ν^2 is order unity. It is further assumed that $\gamma=\sqrt{F^2-1}$ is of order unity. For both inner and outer regions, series expansion solutions of Eq. (1) are sought as

$$u=\epsilon(u_0+\epsilon^{1/2}u_1+\epsilon u_2\ldots),$$
$$v=\epsilon(v_0+\epsilon^{1/2}v_1+\epsilon v_2\ldots), \tag{16}$$
$$\eta=\epsilon(\eta_0+\epsilon^{1/2}\eta_1+\epsilon\eta_2\ldots),$$

where $\eta=\sigma-1+Mh$ is the interface displacement as in Sec. III. Below, the inner solution is given superscript l (linear), and the outer solution superscript f (far field).

Inserting Eq. (16) into Eq. (1) and seeking steady solutions at leading order, the steady nonrotating linear problem is recovered,

$$(F^2-1)\eta_{0xx}^l-\eta_{0yy}^l=-h_{xx}. \tag{17}$$

As discussed in detail elsewhere,[10,12,30] Green's function methods can be used to write the solution of Eq. (17), for right-to-left flow as here, as

$$\eta_0^l(x,y)=\frac{F^2}{2\gamma}\left\{\int_{-\infty}^{y}h_x(x-\gamma(y-\tilde{y}),\tilde{y})d\tilde{y} + \int_{y}^{\infty}h_x(x+\gamma(y-\tilde{y}),\tilde{y})d\tilde{y}\right\}. \tag{18}$$

It is useful at this stage to introduce a rotated coordinate system $(\mathcal{X}_\pm,\mathcal{Y}_\pm)=(x\pm\gamma y, y\mp\gamma x)/F$ for the regions $y>0$ and $y<0$, respectively. In $y>0$, the new coordinate system is rotated anticlockwise through an angle $\tan^{-1}\gamma$ so that $\mathcal{X}_+$ measures distance perpendicular to the Mach lines, $x+\gamma y=$const, and $\mathcal{Y}_+$ the distance along the Mach lines. A similar, but clockwise, rotation occurs for the coordinates in $y<0$. In terms of these new coordinates, Johnson and Vilenski[30] noted that, provided the obstacle height decays sufficiently rapidly at large distances, as $y\to\pm\infty$ solution (18) converges to

$$\lim_{y\to\pm\infty}\eta_0^l(x,y)=\frac{F^2}{2\gamma^2}\int_{-\infty}^{\infty}\begin{cases}h_x\left(\mathcal{X},\dfrac{(F\mathcal{X}_+-\mathcal{X})}{\gamma}\right)d\mathcal{X}, & y\to+\infty\\ h_x\left(\mathcal{X},\dfrac{(\mathcal{X}-F\mathcal{X}_-)}{\gamma}\right)d\mathcal{X}, & y\to-\infty.\end{cases} \tag{19}$$

Equation (19) shows that the linear solution away from the obstacle tends to a function of the single coordinate $\mathcal{X}_\pm$, with sign taken according to whether we are looking at $y\to\pm\infty$. For definiteness, the upper half plane $y>0$ will be considered hereafter (the lower half-plane solution being symmetric), and the subscript + will be dropped.

For the particular case of an axisymmetric obstacle $h=h(r)$, a change in variables allows Eq. (19) to be expressed as[12]

$$\eta_0^l(\mathcal{X}) \to -\frac{1}{\gamma}\mathcal{X}G(\mathcal{X}), \quad \text{where } G(\mathcal{X}) = \int_{|\mathcal{X}|}^{\infty} \frac{h'(r)}{\sqrt{r^2-\mathcal{X}^2}}dr. \tag{20}$$

In the absence of nonlinearity and rotation, the linear wake profile (20) would persist out to $\mathcal{Y}\to\infty$. However, at large $\mathcal{Y}$ it is expected that nonlinear and rotating effects will be important, and consequently it is necessary to match the inner solution (20) with an outer solution to capture these effects. The analysis leading to the outer solution is closely analogous to that used to obtain the governing equation for the wake in dispersive flow past a thin body.[31,32]

Introducing rotated outer coordinates $(\mathcal{X}_*,\mathcal{Y}_*)=\epsilon(\mathcal{X},\mathcal{Y})$, and seeking solutions of Eq. (1) in the outer region away from the obstacle (i.e., where $h\equiv 0$), it becomes clear that derivatives in the $\mathcal{X}$ and $\mathcal{Y}$ directions arise at different orders in ϵ. Consequently, it is found to be natural to seek solutions of the form $\eta=\eta^f(\mathcal{X},\mathcal{Y}_*)$, etc. At leading order, Eq. (1) is found to be satisfied when

$$u_0^f = \frac{\eta_0^f}{F}, \quad v_0^f = \frac{\gamma\eta_0^f}{F},$$

for any $\eta_0^f(\mathcal{X},\mathcal{Y}_*)$. Rotation enters the problem at the next order [$O(\epsilon^{3/2})$ terms] where it is established that

$$u_{1\mathcal{X}}^f = \frac{\eta_{1\mathcal{X}}^f}{F} - \frac{\nu\gamma\eta_0^f}{F^2}, \quad v_{1\mathcal{X}}^f = \frac{\gamma\eta_{1\mathcal{X}}^f}{F} + \frac{\nu\eta_0^f}{F^2}.$$

To find an equation determining η_0^f, it is necessary to proceed to $O(\epsilon^2)$ in the expansion. At this order, terms in η_1^f, η_2^f can be eliminated leaving

$$(2\gamma\eta_{0\mathcal{Y}_*}^f + 3\eta_0^f\eta_{0\mathcal{X}}^f)_{\mathcal{X}} - \nu^2\eta_0^f = 0. \tag{21}$$

Here we will refer to Eq. (21) as the Ostrovsky–Hunter (OH hereafter) equation following Boyd.[33] Ostrovsky[34] derived Eq. (21), including an additional dispersive term, to describe the time evolution of one-dimensional nonlinear inertia-gravity waves (i.e., a rotation modified Korteweg–de Vries equation), and Hunter[35] discusses numerical methods for its solution.

One important point to note regarding Eq. (21) as a description of the supercritical wake is that the outer along Mach-line coordinate $\mathcal{Y}_*$ assumes the role taken by the time-like variable in the previous studies. The "initial" condition for Eq. (21) determined by matching with the inner solution (18) above, is simply the far-field form of that solution

$$\eta_0^f(\mathcal{X},0) = -\frac{1}{\gamma}\mathcal{X}G(\mathcal{X}), \quad \text{where } G(\mathcal{X}) = \int_{|\mathcal{X}|}^{\infty} \frac{h'(r)}{\sqrt{r^2-\mathcal{X}^2}}dr. \tag{22}$$

For the case of the WA obstacle (see Table I), $G(\mathcal{X})$ can be evaluated directly to be

$$G(\mathcal{X}) = -\frac{2}{a(1+(\mathcal{X}/a)^2)^2}. \tag{23}$$

ERJ07a (Ref. 12) gave explicit expressions for $G(\mathcal{X})$ for the other obstacles in Table I.

Recalling that $\nu=\sqrt{B/M}$, Eq. (21) together with Eq. (22) can be rescaled [defining $\phi=(3/\nu^2)\eta_0^f$, $\tau=(\nu^2/2\gamma)\mathcal{Y}_*$] into the canonical problem

$$(\phi_\tau + \phi\phi_{\mathcal{X}})_{\mathcal{X}} - \phi = 0, \quad \text{with } \phi(\mathcal{X},0) = \phi_0(\mathcal{X}) = -\beta\mathcal{X}G(\mathcal{X}). \tag{24}$$

The single parameter appearing in Eq. (24) is

$$\beta = \frac{3M}{B\sqrt{F^2-1}}. \tag{25}$$

For a given obstacle then, it is clear from Eq. (24) that the essential structure of its wake in supercritical, rotating flow is a function solely of β.

B. Numerical solution of the Ostrovsky–Hunter equation

In the absence of analytical results for the OH equation, numerical calculations are required to examine the wake behavior. Two different numerical methods have been employed, namely a spectral method using characteristic variables, and a finite volume discretization. The spectral method allows the onset of wave breaking to be defined precisely, and consequently accurate calculation of the location in the $(\mathcal{X},\tau)$-plane where breaking first occurs, as a function of β, is made possible. The finite volume method is used to follow the solution long after breaking occurs, when the spectral technique would become prohibitively expensive. A further advantage of using two methods is that they act to cross-validate one another.

The spectral method is formulated by first transforming Eq. (24) to the usual characteristic coordinates q, s with $\tau(q,s)=s$ and $\mathcal{X}(q,s)$ defined by

$$\frac{\partial\mathcal{X}}{\partial s} = \phi(\mathcal{X}(q,s),s), \quad \mathcal{X}(q,0) = q.$$

Under this change in variables Eq. (24) is transformed to the set

$$\phi_{qs} = \psi\phi, \quad \phi_q(q,0) = \phi_0'(q), \qquad \psi_s = \psi\phi_q, \quad \psi(q,0) = 1, \tag{26}$$

where $\psi\equiv\partial\mathcal{X}/\partial q$ is the Jacobian of the mapping between the original $(\mathcal{X},\tau)$ and characteristic (q,s) coordinates. Together with the boundary condition $\phi(-\infty,s)=0$, set (26) can be integrated forward in s using a pseudospectral method. The solution is written as a series in Chebyshev polynomials with time-dependent coefficients, e.g.,

$$\phi(q,s) = \sum_{k=0}^{N} a_k(s)T_k(q), \text{ etc.}$$

Collocation at the grid points $q_j=\pi(-1+2j/N)$, $j=0,\ldots,N-1$ converts the system of partial differential equations into a set of coupled ordinary differential equations (in s) for the coefficients $a_k(s)$ which are easily solved via a fourth order Runge–Kutta method.

The advantage of the spectral formulation is the following. When wave breaking occurs we have $\phi_{\mathcal{X}}\to-\infty$. In the

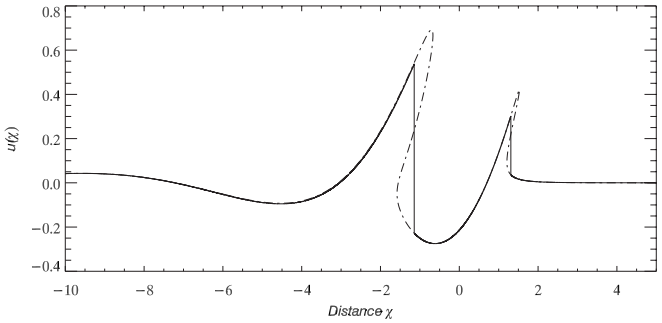

FIG. 3. Comparison of numerical solutions to the OH Eq. (24) using spectral and finite volume methods discussed in the text. The initial condition was taken to be that corresponding to the WA obstacle [see Eq. (23)]. The similarity parameter $\beta=1$; the solution shown is for $\tau=2.6$. The solid line shows the CLAWPACK shock fitting solution, with spatial resolution $\delta\mathcal{X}=0.000\,05$. The broken line shows the pseudospectral parametric solution for the same problem, computed using 1024 Chebyshev nodes.

parametric form (26) since $\phi_{\mathcal{X}}=\phi_q/\psi$, this corresponds to the Jacobian becoming singular, i.e., $\psi=0$. Thus the onset of wave breaking, one of the diagnostics of interest here, may be diagnosed by an order one quantity passing through zero, as opposed to a gradient approaching infinity.

The disadvantage of the spectral method is that it becomes expensive to continue the calculations for very long after wave breaking has taken place. In order to compare the OH solutions to those of the full nonlinear rSWE, a finite volume method is also employed. This is achieved by extending the method, described by LeVeque,[18] to solve the Hopf equation

$$\phi_\tau+\phi\phi_{\mathcal{X}}=0, \tag{27}$$

using the CLAWPACK finite volume package, with the usual weak solutions, satisfying

$$-V[\phi]_-^+ + \tfrac{1}{2}[\phi^2]_-^+ = 0,$$

permitted for discontinuities in $\mathcal{X}$ propagating at speed V. Integrating Eq. (24) in $\mathcal{X}$, the OH equation becomes the Hopf Eq. (27) with an additional source term. The source term is treated using Strang splitting, exactly as for the rotating terms in full rSWE solutions described above.

Figure 3 shows a comparison between solutions generated by the two numerical methods (see caption for details). A snapshot is shown for a calculation with initial condition as for the WA obstacle (23) and with the parameter $\beta=1$. The "time" (τ) of the snapshot is chosen to show the situation after wave breaking has occurred, but before the breaking waves have developed to cause the pseudospectral method to become prohibitively expensive. Agreement between the two methods is seen to be good, with the finite volume code having fitted "equal area" hydraulic jumps[27] at the breaking waves.

C. Comparison with rotating shallow water flows

Next, solutions of the OH Eq. (24) for the wave field will be compared to those from the full rSWE (1). The advantage of the OH representation is that a three parameter problem (F,M,B) in the rSWE becomes a single parameter problem (β) in the OH representation. The comparison will serve to test accuracy of the OH representation at finite M, a necessary test of its utility as it is formally valid only for $M\ll 1$.

Figure 4 compares the steady interface displacements $\eta(x,y)$ obtained from four separate solutions of the rSWE with those derived from a single solution of the OH Eq. (24), with $\beta=0.5$. To reconstruct a displacement height field $\eta_{\mathrm{OH}}(x,y)$, for the upper half plane $y>0$, from a solution $\phi(\mathcal{X},\tau)$ of Eq. (24), the inverse mapping and rescaling

$$\eta_{\mathrm{OH}}(x,y)=\frac{B}{3}\phi\left(\frac{x+\gamma y}{F},\frac{B(y-\gamma x)}{2F\sqrt{F^2-1}}\right) \tag{28}$$

can be applied. It is important to note that, although a given OH solution $\phi(\mathcal{X},\tau)$ depends only on β, the mapping Eq. (28) depends on each on the parameters (F,M,B) of the corresponding rSWE flow. Note also that since the OH solution describes the evolution of the wave field along a single Mach line emanating from the obstacle, and must be matched to the linear solution in the vicinity of the obstacle itself, it is meaningful to plot the resulting solution $\eta_{\mathrm{OH}}(x,y)$ only for $y\geq 1$ in Fig. 4. Symmetry considerations allow this solution to be reflected about $y=0$, allowing the solution for $y\leq -1$ also to be plotted.

The parameter dependence of the inverse mapping Eq. (28) is not immediately obvious and it turns out that wave fields that appear superficially to be rather different can be generated from a single solution of Eq. (24). The specific $\eta_{\mathrm{OH}}(x,y)$ fields plotted in Fig. 4 (middle columns) are generated from a single solution of Eq. (24) with $\beta=0.5$, but different parameter triplets (F,M,B) corresponding to full integrations of the rSWE, are used to map the solution back into the physical domain. The final steady state $\eta(x,y)$ fields from separate rSWE integrations at these parameter settings are plotted in Fig. 4 (left column). If the top row in Fig. 4 is regarded as a control experiment, then the remaining rows show integrations in which the three pairs of parameters (M,F), (F,B), and (M,B) are varied in turn while keeping β constant. Good qualitative and quantitative agreement between the rSWE and OH solutions is evident in each case, within the regions $|y|>1$ where the comparison is valid. Cross sections of the interface displacement field $\eta(x,y)$ at fixed values of y are shown in the right column for each set of integrations.

An interesting finite obstacle height (finite M) effect is that the rSWE solutions are not symmetric about $y=0$, so for the rSWE solutions the cross sections are plotted for $y=\pm$ const. The dynamical cause of the symmetry breaking in the wake of the obstacle in the rSWE solutions is due to the generation of relative vorticity at the obstacle (i.e., topographic vorticity), and its associated circulation. Conservation of potential vorticity of the flow over the obstacle reveals that the relative vorticity has magnitude $\sim\sqrt{B}M$ (the relevant units being cL^{-1}). Symmetry breaking is therefore not present in the OH limit $M,\ B\to 0$, as it remains a high order effect compared to the modifications to the obstacle wake on long length scales due to nonlinearity and rotation-induced long-wave dispersion. The asymmetry about $y=0$ is

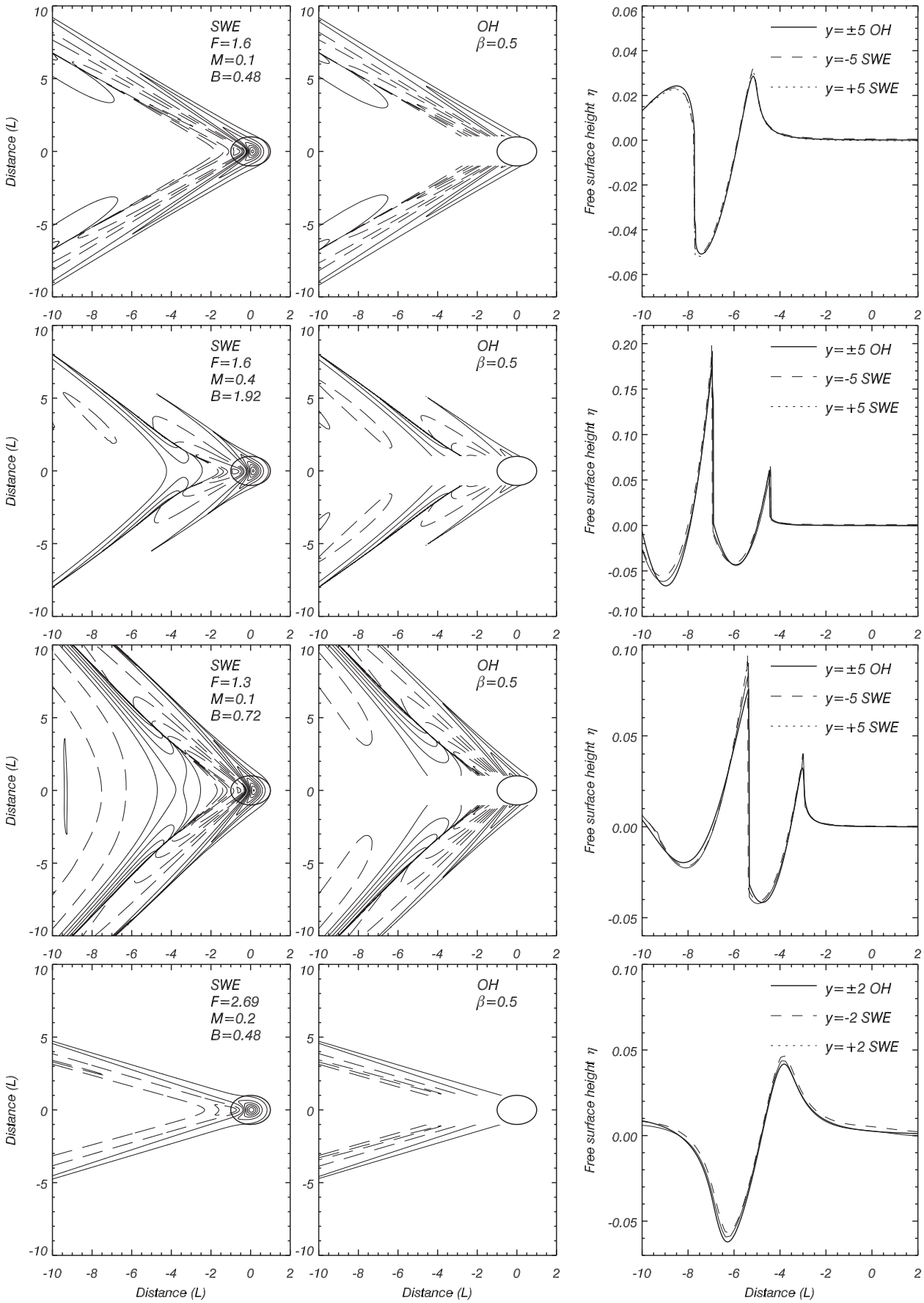

FIG. 4. Left column: the steady interface displacement field $\eta(x,y)$ for four different rSWE flows over the WA obstacle at the given parameter settings (each corresponding to β=0.5). Contour intervals in each panel are $0.15M$, with negative contours dashed and the zero contour omitted. Center column: the solution $\phi(\mathcal{X},\mathcal{Y}_*)$ of the OH equation with β=0.5, mapped back into the physical domain under Eq. (28) for comparison with the corresponding rSWE flow. Right column: Cross sections of the rSWE and OH displacement height fields at fixed cross-stream distance $y=\pm$constant from the obstacle.

seen in Fig. 4 to be very weak, at least for those values of M corresponding to the present cases. In each case the OH solution accurately reproduces the location and magnitude of the hydraulic jumps present in the rSWE solution.

D. The location of the onset of wave breaking

Based on the results above, it appears reasonable to take the OH Eq. (24) as a quantitative model for rSWE supercritical wakes. The aim next is to find a simple expression, based on the OH approximation, for the spatial location of the onset of wave breaking in the wake. The question of interest here is how far, in terms of obstacle radii, the waves propagate along the Mach lines before wave breaking occurs. The resulting "breaking distance" provides an important constraint on the horizontal distance across which along-stream momentum can be transported by the waves.

To derive the breaking distance, we first define $\tau=\tau_b$ to be the lowest value of the along Mach-line coordinate τ at which wave breaking is detected, in integrations of the canonical OH Eq. (24). The value taken by τ_b depends on both β and the obstacle shape, both of which enter the problem in the initial conditions of Eq. (24). Equation (24) is integrated numerically using the spectral method, for a series of values of β, in order to calculate $\tau_b(\beta)$. As described above, the spectral method provides an objective numerical definition of "breaking." For initial conditions corresponding to common obstacles, two separate occurrences of breaking can be found using this method [i.e., two separate values of $\tau_b(\beta)$]. The first corresponds to wave breaking toward the rear of the obstacle wake, and the second, which invariably occurs at a larger value of τ corresponds to the onset of (rather weaker) wave breaking near the front of the wake (see also Fig. 4).

Figure 5 shows the functions $\tau_b(\beta)$ for two different obstacles, the Gaussian and WA. The function $\tau_b(\beta)$ determining the onset position of the front shocks for each obstacle is plotted as a solid curve, and the rear shock as a dashed curve. At large β each curve asymptotes to a function $\tau_b^\infty(\beta)$, specific to each obstacle, plotted on Fig. 5 as dotted curves. The large β limit corresponds to the absence of rotation, and in this case the nonrotating breaking times can be determined from the solution of the Hopf equation[27] (27) with initial condition as in Eq. (24). It is straightforward to show that this distance is, for both front and rear shocks,

$$\tau_b^\infty = \frac{1}{\beta \max[G(\mathcal{X}) + \mathcal{X}G'(\mathcal{X})]}.$$

At lower values of β, rotation acts to increase the distance at which the front wave is seen to break, and decrease that of the rear. Even for $\beta=0.5$, however, the breaking distances have changed from the nonrotating value by a factor of less than 2. The location where the front and rear jumps (or shocks) first form is remarkably independent of obstacle type. Using the mapping Eq. (28) to convert back to a physical distance D_b from the obstacle (units are the obstacle nondimensional length scale) gives

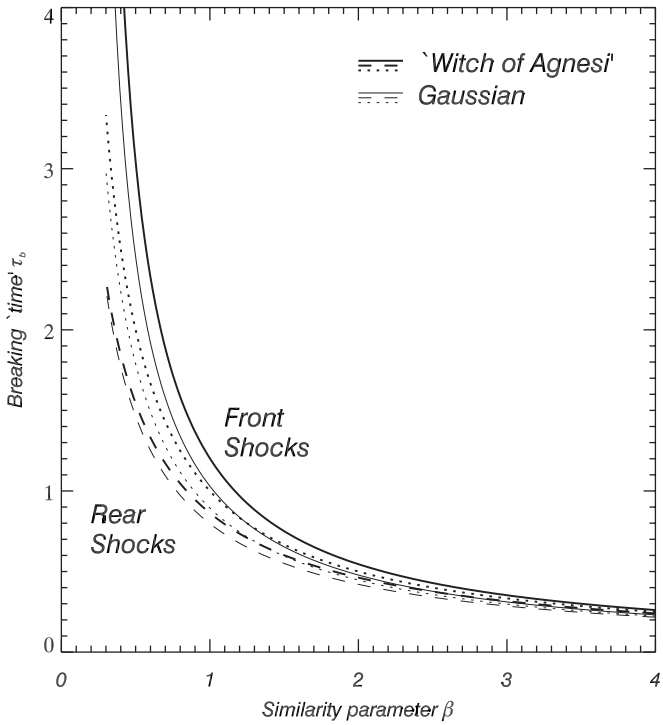

FIG. 5. Illustrating the time $\tau=\tau_b$ at which a shock first forms in the OH solutions, plotted as a function of the free parameter β, when the initial conditions (specified at $\tau=0$) are as for the WA and Gaussian obstacles. Both front shocks (solid) and rear shocks (dashed) are shown. Dotted curves show the corresponding times for both front and rear shocks in nonrotating flow.

$$D_b = \frac{2\sqrt{F^2-1}}{B}\tau_b(\beta) \quad \left(\beta = \frac{3M}{B\sqrt{F^2-1}}\right),$$
$$D_b^\infty = \frac{2(F^2-1)}{3M \max[G(\mathcal{X}) + \mathcal{X}G'(\mathcal{X})]}. \tag{29}$$

Equation (29) in combination with Fig. 5 allows straightforward estimation of the onset location of wave breaking in supercritical rotating shallow water flow over topography. The expression for D_b^∞ is the corresponding nonrotating result derived from τ_b^∞.

V. CONCLUSIONS

In the introduction two key questions were posed on the topic of rotating, supercritical, one-and-a-half-layer shallow flow over topography. The meteorological scenario for which our results are directly relevant is that of a shallow neutral layer under a sharp inversion, with a deep layer above and with relatively weak wind shear between the two layers.

The answer to the first question, concerning what determines the drag exerted by the obstacle on the flow, is that an exact formula (12) derived from linear theory, expresses the dependence of the drag on the three flow parameters (F,M,B). Numerical simulations of nonlinear flows demonstrated that this formula remains accurate throughout the supercritical regime, up to obstacle heights of at least $M \approx 0.7$. The linear theory gives accurate results for the drag over relatively high obstacles because nonlinear effects are displaced to the wake at the obstacle flanks and consequently do

not significantly affect drag. One interesting feature of the drag function is that rotation may act to increase drag (see Fig. 2). Numerical simulations of rotating stratified flow[5,6] suggest that drag due to vertically propagating waves is decreased by the presence of rotation so the increase in drag due to rotation found here appears to be associated with the excitation of vertically trapped waves.

The answer to the second question, concerning what determines the location of wave breaking in the wake behind the obstacle, has been answered by demonstrating that the wake structure can be accurately modeled, at least for low to moderate obstacle heights and relatively weak rotation, by the weakly nonlinear OH Eq. (24). In nonrotating flows two hydraulic jumps are formed at an identical distance from the obstacle in the wake to each side. Rotation affects the onset of wave breaking by introducing dispersion at the long wavelength end of the excited spectrum. The net effect of this long-wave dispersion is to cause the rear hydraulic jump to form closer to the obstacle, but the front hydraulic jump to form further away. The dispersion opposes nonlinear wave steepening effects for the front wave, although it appears that in most cases short waves, which are relatively unopposed by dispersion and typically of small amplitude, will eventually steepen and break (cf. the microbreaking of Boyd[33]). Consideration of the OH formulation leads to Eq. (29), which expresses the distance along the Mach lines that breaking waves will first be encountered as a function of the initial flow parameters.

The conclusion of the present work that in supercritical flows the rear hydraulic jumps increase in amplitude and move closer to the obstacle, whereas the upstream hydraulic jumps decrease in amplitude and move further away, is fully consistent with the results of experimental, analytical and numerical works that consider the transcritical regime.[11,13,36] The rotating towing-tank experiments of Johnson *et al.*[36] demonstrated that transcritical rotating flows feature a "sharp-crested" nonlinear wave to the rear of the obstacle that is not present in nonrotating flow. In transcritical two-dimensional flow over a ridge, the analytical results of Esler *et al.*[11] showed that increasing rotation leads to the appearance and growth of a hydraulic jump downstream of the obstacle that can exceed the amplitude of the upstream jump. The regime diagram of ERJ07b (Ref. 13) (their Fig. 4) shows that three-dimensional rotating transcritical flows (with $1 < F \lesssim 1+\Gamma^{+}M^{2/3}$) over isolated obstacles are dominated by rear hydraulic jumps at high rotation rates, and front jumps when rotation is weak. The overall conclusion that rotation acts to generate and/or amplify rear hydraulic jumps and tends to suppress upstream jumps therefore appears to be robust across a range of flow geometries and flow speeds.

The present results have been obtained under the assumption, following the discussion in Sec. II, that mass and lower layer momentum are conserved across hydraulic jumps. The resulting jump condition (2) models the situation at a turbulent breaking wave at an internal standing hydraulic jump. There has been much discussion in literature[15,17] about the correct conditions to apply at different types of internal jumps and bores, and it should be borne in mind that are results are likely to show some quantitative sensitivity to the type of jump condition used.

It is hoped that the results presented here will assist in the interpretation of numerical simulations of more realistic flows over topography in which trapped waves are excited.[5,6] Further, the results may be of use in the design and implementation of gravity wave drag parametrizations for climate models for which rotating effects are important.

APPENDIX A: EVALUATION OF INTEGRAL (11)

In this appendix the evaluation of the integral

$$I(\kappa;F,B) = \lim_{\epsilon\to 0} \int_0^{2\pi} \frac{\cos\theta(B-\kappa^2F^2\cos^2\theta)}{-\kappa^2F^2\cos\theta + B + \kappa^2 - 2i\epsilon\kappa F\cos\theta} d\theta \tag{A1}$$

is described. The integral can be evaluated using the standard complex substitution $z=e^{i\theta}$ and integrating anticlockwise around the unit circle in the complex plane $\{C:|z|=1\}$. A similar integral has been evaluated in the nonrotating context using this substitution by Jiang and Smith.[10]

Adopting the substitution, after some algebra the integral can be written as

$$I(\kappa;F,B) = \lim_{\tilde{\epsilon}\to 0} \oint_C \frac{(A^2(z^2+1)^2 - 4R^2z^2)(z^2+1)}{A^2(z^2+1)^2 - 4z^2 + i\tilde{\epsilon}z(z^2+1)} \frac{dz}{2iz^2}, \tag{A2}$$

where

$$A^2 = \frac{\kappa^2F^2}{B+\kappa^2}, \quad R^2 = \frac{B}{B+\kappa^2}. \tag{A3}$$

For $\tilde{\epsilon}=0$ and $A<1$ the five poles of the integrand can be shown to lie on the real axis, and the resulting integral can be shown to be zero. For $A>1$ and $\tilde{\epsilon}=0$ the five poles are located at $z=z_i$, $i=1$ and 5,

$$z_1 = e^{i\alpha}, \quad z_2 = e^{i(\pi-\alpha)}, \quad z_3 = e^{i(\pi+\alpha)}, \quad z_4 = e^{i(2\pi-\alpha)}, \quad z_5 = 0, \quad \text{with } \alpha = \tan^{-1}\{\sqrt{A^2-1}\}, \tag{A4}$$

and with z_{1-4} simple poles and z_5 a double pole. Next, we need to examine what happens to the location of the poles on the unit circle z_{1-4} when $\tilde{\epsilon}$ is nonzero. For small $\tilde{\epsilon}$ each pole z_i will be displaced slightly to a new location $z_i+\tilde{\epsilon}w_i + O(\tilde{\epsilon}^2)$. Inserting into the expression

$$A^2(z^2+1)^2 - 4z^2 + i\tilde{\epsilon}z(z^2+1) = 0, \tag{A5}$$

equating terms in $\tilde{\epsilon}$ and using the fact that

$$A^2(z_i^2+1)^2 - 4z_i^2 = 0, \tag{A6}$$

the following expression is arrived at

$$w_i = -\frac{z_i}{4A^2\sin\{\mathrm{Arg}(z_i)\}}. \tag{A7}$$

Clearly the correction term w_i is proportional to z_i in each case, and therefore the sign of the (real) constant of proportionality determines whether each pole moves in or out of the unit circle. Hence we deduce that for $\tilde{\epsilon}>0$, z_1 and z_2 move

inside the unit circle and z_3 and z_4 move outside. The integral for $A>1$ is therefore given by

$$I(\kappa;F,B) = 2\pi i[\mathrm{Res}(z_1) + \mathrm{Res}(z_2) + \mathrm{Res}(z_5)]. \tag{A8}$$

For the double pole at $z_5=0$,

$$\mathrm{Res}(z_5) = \frac{d}{dz}\left.\frac{1}{2i}\frac{(A^2(z^2+1)^2 - 4R^2z^2)(z^2+1)}{A^2(z^2+1)^2 - 4z^2}\right|_{z=0} = 0. \tag{A9}$$

For the remaining poles

$$\begin{aligned}\mathrm{Res}(z_1) &= \left.\frac{1}{2i}\cdot\frac{(A^2(z^2+1)^2 - 4R^2z^2)(z^2+1)}{A^2(z-z_2)(z-z_3)(z-z_4)}\right|_{z=z_1} \\ &= \frac{\cos^2\alpha - (R/A)^2}{2\sin\alpha} = \frac{1-R^2}{2A\sqrt{A^2-1}} \\ &= \frac{1}{2F\sqrt{F^2-1}}\frac{\kappa}{\sqrt{\kappa^2 - B/(F^2-1)}},\end{aligned} \tag{A10}$$

and $\mathrm{Res}(z_2)=\mathrm{Res}(z_1)$. Hence

$$I(\kappa;F,B) = \begin{cases} \dfrac{2\pi i}{F\sqrt{F^2-1}}\dfrac{\kappa}{\sqrt{\kappa^2 - B/(F^2-1)}}, & \text{for } A>1 \\ 0, & \text{for } A<1. \end{cases} \tag{A11}$$

APPENDIX B: EQUIVALENCE OF THE TWO EQUATIONS FOR DRAG IN NONROTATING FLOW

Here and in Ref. 12 two separate expressions have been obtained for the drag on an obstacle in nonrotating shallow water flow. The implication of the two separate results is that

$$2\int_0^\infty G(\mathcal{X})^2\mathcal{X}^2 d\mathcal{X} = \pi\int_0^\infty \kappa^2\hat{h}(\kappa)^2 d\kappa, \tag{B1}$$

where

$$G(\chi) = \int_{\mathcal{X}}^\infty \frac{h'(r)}{\sqrt{r^2-\mathcal{X}^2}}dr$$

and

$$\hat{h}(\kappa) = \int_0^\infty h(r)J_0(\kappa r) r\ dr. \tag{B2}$$

Here we show that this result, which can be viewed as a variation on Parseval's theorem for Fourier–Bessel transforms, in fact holds.

First note that the integral on the right-hand side can be written as

$$\begin{aligned}&\pi\int_0^\infty \kappa^2\hat{h}(\kappa)^2 d\kappa \\ &= \pi\int_0^\infty\int_0^\infty\int_0^\infty h(r)h(s)J_0(r\kappa)J_0(s\kappa)\kappa^2 rs\,dr\,ds\,d\kappa \\ &= 2\pi\int_0^\infty\int_s^\infty\int_0^\infty h'(r)h'(s)J_1(r\kappa)J_1(s\kappa)rs\,d\kappa\,dr\,ds \quad (s<r) \\ &= 4\int_0^\infty\int_s^\infty h'(r)h'(s)r\left[K\left(\frac{s^2}{r^2}\right) - E\left(\frac{s^2}{r^2}\right)\right]dr\,ds,\end{aligned} \tag{B3}$$

where $K(z)$ and $E(z)$ are the complete elliptic integrals of the first and second kinds respectively. To obtain this result integration by parts in r and s is first used, utilizing the result

$$\int J_0(r\alpha)\alpha r dr = rJ_1(r\alpha). \tag{B4}$$

Symmetry in r and s is then used to restrict the domain of integration to $r>s$. Finally, the integral in κ is evaluated using the identity

$$\int_0^\infty J_1(\alpha z)J_1(\beta z)dz = \frac{2}{\alpha\pi}\left[K\left(\frac{\alpha^2}{\beta^2}\right) - E\left(\frac{\alpha^2}{\beta^2}\right)\right] \quad (\alpha<\beta). \tag{B5}$$

For the second integral, similarly,

$$\begin{aligned}&2\int_0^\infty \mathcal{X}^2 G(\mathcal{X})^2 d\mathcal{X} \\ &= 2\int_0^\infty\int_{\mathcal{X}}^\infty\int_{\mathcal{X}}^\infty \frac{h'(r)h'(s)\mathcal{X}^2}{\sqrt{r^2-\mathcal{X}^2}\sqrt{s^2-\mathcal{X}^2}}dr\,ds\,d\mathcal{X} \\ &= 4\int_0^\infty\int_s^\infty\int_0^s \frac{h'(r)h'(s)\mathcal{X}^2}{\sqrt{r^2-\mathcal{X}^2}\sqrt{s^2-\mathcal{X}^2}}d\mathcal{X}\,dr\,ds \quad (s<r) \\ &= 4\int_0^\infty\int_s^\infty h'(r)h'(s)r\left[K\left(\frac{s^2}{r^2}\right) - E\left(\frac{s^2}{r^2}\right)\right]dr\,ds.\end{aligned} \tag{B6}$$

Note that in this case, change in the order of integration requires care to be taken with the limits of the integrals. Again, symmetry in r and s is exploited to restrict the domain of integration to $r>s$. The standard definitions of the elliptic integrals can then be manipulated to obtain the following result used in the evaluation of the $\mathcal{X}$ integral,

$$\int_0^\alpha \frac{\mathcal{X}^2}{\sqrt{\beta^2-\mathcal{X}^2}\sqrt{\alpha^2-\mathcal{X}^2}}d\mathcal{X} = \beta\left[K\left(\frac{\alpha^2}{\beta^2}\right) - E\left(\frac{\alpha^2}{\beta^2}\right)\right] \quad (\alpha<\beta). \tag{B7}$$

Clearly, there is equality between the two integral expressions and the result is proved.

[1] J. W. Rottman and F. Einaudi, "Solitary waves in the atmosphere," J. Atmos. Sci. **50**, 2116 (1993).
[2] J. W. Rottman and R. H. J. Grimshaw, in *Environmental Stratified Flows* (Kluwer, Boston, 2001), Chap. 3, pp. 61–88.
[3] K. R. Helfrich and W. K. Melville, "Long nonlinear internal waves," Annu. Rev. Fluid Mech. **38**, 395 (2006).
[4] X. F. Li, C. M. Dong, P. Clemente-Colon, W. G. Pichel, and K. S. Friedman, "Synthetic aperture radar observation of the sea surface imprints of up-stream atmospheric solitons generated by flow impeded by an island," J. Geophys. Res. **209**, 1029 (2004).
[5] P. M. A. Miranda and I. N. James, "Nonlinear three-dimensional effects on gravity-wave drag: Splitting flow and breaking waves," Q. J. R. Meteorol. Soc. **118**, 1057 (1992).
[6] H. Olafsson and P. Bougeault, "The effect of rotation and surface friction on orographic drag," J. Atmos. Sci. **54**, 193 (1997).
[7] Note, however, that the definition of Froude number differs for stratified flow, where it is U/Nh_m, with N buoyancy (Brunt–Väisälä) frequency, U the oncoming flow speed, and h_m the topographic height scale as here.

[8]C. Schär and R. B. Smith, "Shallow water flow past an isolated topography. Part I: Vorticity production and wake formation," J. Atmos. Sci. **50**, 1373 (1993a).
[9]C. Schär and R. B. Smith, "Shallow water flow past an isolated topography. Part II: Transition to vortex shedding," J. Atmos. Sci. **50**, 1401 (1993b).
[10]Q. Jiang and R. B. Smith, "V-waves, bow shocks, and wakes in supercritical hydrostatic flow," J. Fluid Mech. **406**, 27 (2000).
[11]J. G. Esler, O. J. Rump, and E. R. Johnson, "Steady rotating flows over a ridge," Phys. Fluids **17**, 116601 (2005).
[12]J. G. Esler, O. J. Rump, and E. R. Johnson, "Nondispersive and weakly dispersive single layer flow over an axisymmetric obstacle: The equivalent aerofoil formulation," J. Fluid Mech. **574**, 209 (2007a).
[13]J. G. Esler, O. J. Rump, and E. R. Johnson, "Transcritical rotating flow over topography," J. Fluid Mech. **590**, 81 (2007b).
[14]D. D. Houghton, "Effect of rotation on the formation of hydraulic jumps," J. Geophys. Res. **74**, 1351, DOI: 10.1029/JB074i006p01351 (1969).
[15]J. B. Klemp, R. Rotunno, and W. C. Skamarock, "On the propagation of internal bores," J. Fluid Mech. **331**, 81 (1997).
[16]J. S. Turner, *Buoyancy Effects in Fluids* (Cambridge University Press, Cambridge, 1973).
[17]P. G. Baines, *Topographic Effects in Stratified Flows* (Cambridge University Press, Cambridge, 1995).
[18]R. J. LeVeque, *Finite Volume methods for Hyperbolic Problems* (Cambridge University Press, Cambridge, 2002).
[19]A. Kuo and L. M. Polvani, "Time-dependent fully nonlinear geostrophic adjustment," J. Phys. Oceanogr. **27**, 1614 (1997).
[20]F. Bouchut, J. Le Sommer, and V. Zeitlin, "Frontal geostrophic adjustment and nonlinear wave phenomena in one-dimensional rotating shallow water. Part II. High resolution numerical simulations," J. Fluid Mech. **514**, 35 (2004).
[21]E. Audusse, F. Bouchut, M.-O. Bristeau, R. Klein, and B. Perthame, "A fast and stable well-balanced scheme with hydrostatic reconstruction for shallow water flows," SIAM J. Sci. Comput. (USA) **25**, 2050 (2004).
[22]O. J. Rump, "Non-rotating and rotating free surface flows over topography," Ph.D. thesis, University of London, 2007.
[23]G. G. Vilenski and E. R. Johnson, "Near critical free-surface rotating flow over topography," Proc. R. Soc. London, Ser. A **460**, 2865 (2004).
[24]B. B. Kadomtsev and V. I. Petviashvili, "On the stability of solitary waves in weakly dispersing media," Sov. Phys. Dokl. **15**, 539 (1970).
[25]R. H. J. Grimshaw and W. K. Melville, "On the derivation of the modified Kadomtsev-Petviashvili equation," Stud. Appl. Math. **80**, 183 (1989).
[26]P. M. Morse and H. Feshbach, *Methods of Theoretical Physics, Parts I and II* (McGraw-Hill, New York, 1953).
[27]G. B. Whitham, *Linear and Nonlinear Waves* (Wiley, New York, 1974).
[28]M. J. Lighthill, "Group velocity," J. Inst. Math. Appl. **1**, 1 (1965).
[29]I. S. Gradshteyn and I. M. Ryzhik, *Table of Integrals, Series and Products* (Academic, New York, 1965).
[30]E. R. Johnson and G. G. Vilenski, "Flow patterns and drag in near-critical flow over isolated orography," J. Atmos. Sci. **61**, 2909 (2004).
[31]A. V. Gurevich, A. L. Krylov, V. V. Khodorovsky, and G. A. El, "Supersonic flow past bodies in dispersive hydrodynamics," J. Exp. Theor. Phys. **80**, 87 (1995).
[32]A. V. Gurevich, A. L. Krylov, V. V. Khodorovsky, and G. A. El, "Supersonic flow past finite-length bodies in dispersive hydrodynamics," J. Exp. Theor. Phys. **82**, 709 (1996).
[33]J. P. Boyd, "Microbreaking and polycnoidal waves in the Ostrovsky-Hunter equation," Phys. Lett. A **338**, 36 (2005).
[34]L. A. Ostrovsky, "Nonlinear internal waves in a rotating ocean," Oceanology (Engl. Transl.) **18**, 181 (1978).
[35]J. K. Hunter, "Numerical solution of some nonlinear dispersive wave equations," Lect. Appl. Math. **26**, 301 (1990).
[36]E. R. Johnson, J. G. Esler, O. J. Rump, J. Sommeria, and G. G. Vilenski, "Orographically generated nonlinear waves in rotating and nonrotating two-layer flow," Proc. R. Soc. London, Ser. A. **462**, 3 (2006).